

## Three Dimensional Variable-Wavelength X-Ray Bragg Coherent Diffraction Imaging

W. Cha,<sup>1</sup> A. Ulvestad,<sup>1</sup> M. Allain,<sup>2</sup> V. Chamard,<sup>2</sup> R. Harder,<sup>3</sup> S. J. Leake,<sup>4</sup> J. Maser,<sup>3</sup> P. H. Fuoss,<sup>1</sup> and S. O. Hruszkewycz<sup>1,\*</sup>

<sup>1</sup>Materials Science Division, Argonne National Laboratory, Argonne, Illinois 60439, USA

<sup>2</sup>Aix-Marseille University, CNRS, Centrale Marseille, Institut Fresnel, 13013 Marseille, France

<sup>3</sup>X-ray Science Division, Argonne National Laboratory, Argonne, Illinois 60439, USA

<sup>4</sup>ESRF—The European Synchrotron, CS 40220, 38043 Grenoble Cedex 9, France

(Received 15 September 2016; published 23 November 2016)

We present and demonstrate a formalism by which three-dimensional (3D) Bragg x-ray coherent diffraction imaging (BCDI) can be implemented without moving the sample by scanning the energy of the incident x-ray beam. This capability is made possible by introducing a 3D Fourier transform that accounts for x-ray wavelength variability. We demonstrate the approach by inverting coherent Bragg diffraction patterns from a gold nanocrystal measured with an x-ray energy scan. Variable-wavelength BCDI will expand the breadth of feasible *in situ* 3D strain imaging experiments towards more diverse materials environments, especially where sample manipulation is difficult.

DOI: 10.1103/PhysRevLett.117.225501

In materials, nanoscale distributions of strain and lattice distortions in crystals often dictate performance and properties [1], but are difficult to measure under realistic working conditions. Increasingly, Bragg coherent x-ray diffraction imaging (BCDI) is being utilized at synchrotron sources to address this challenge by nondestructively imaging nanoscale strain fields in crystalline materials in three dimensions (3D) using penetrating hard x-rays [2–7]. While these studies have shown great promise, the breadth of feasible 3D BCDI measurements could expand substantially if current experimental requirements such as sample rotation could be eliminated without sacrificing imaging capability.

In a Bragg diffraction experiment, the reciprocal space volume about a Bragg peak can be measured by finely scanning the wavelength of the incident beam (as opposed to its relative angle). Recent investigations have successfully mapped 3D Bragg peaks from crystals in this manner [8–10], but numerical phase retrieval and inversion of such measurements into 3D real space images have yet to be demonstrated. This capability would enable new strain imaging studies of materials in environments where sample manipulation is difficult and the details of nanoscale strain distribution and evolution remain elusive—for example, during high-temperature crystal synthesis.

Here, we present a new variable-wavelength BCDI (vwBCDI) approach that reconstructs a 3D image of strain and density of a crystalline nanoparticle from x-ray energy scan measurements, eliminating the need to rotate the sample. To reconstruct 3D images from this type of data, we introduce a new phase-retrieval approach designed to handle x-ray wavelength ( $\lambda$ ) variability in BCDI, and we demonstrate the method with experimental data.

Using BCDI, lattice distortions within a 3D nanocrystal can be determined from the coherent diffraction intensity distribution about a Bragg peak [4,11]. A typical monochromatic BCDI experiment is shown schematically in

Fig. 1(a), which depicts a nanocrystal ( $\rho$ ) that is illuminated with a coherent x-ray plane wave. The incident beam wave vector  $\mathbf{k}_i$ , exit beam wave vector  $\mathbf{k}_f$ , and nanocrystal are oriented such that the scattering vector  $\mathbf{q} = \mathbf{k}_f - \mathbf{k}_i$  is in the vicinity of a Bragg reflection at the reciprocal lattice point  $\mathbf{G}_{\text{HKL}}$ . (Here,  $|\mathbf{k}| = 2\pi/\lambda$ .) The 3D intensity distribution surrounding the  $\mathbf{G}_{\text{HKL}}$  Bragg peak from  $\rho$  is shown schematically in Fig. 1(b) as a yellow isosurface. Near the Bragg condition, an area detector will measure a cut through this 3D intensity distribution along the plane normal to  $\mathbf{k}_f$  that intersects  $\mathbf{q}$  [12,13]. Different slices can be measured by varying  $\mathbf{Q} \equiv \mathbf{q} - \mathbf{G}_{\text{HKL}}$ , the reciprocal space distance from the center of the area detector to the Bragg peak. As shown in Fig. 1(a), in a typical single-wavelength experiment,  $\mathbf{Q}$  changes over the course of a scan of the sample angle  $\theta$  ( $\pm \sim 0.5^\circ$ ) while  $|\mathbf{q}|$  remains fixed. Such an angle scan (rocking curve) is depicted in Fig. 1(b) as a series of parallel grey planes slicing through the 3D Bragg peak intensity distribution. Thus, the Bragg 3D intensity distribution is recorded slice by slice. The oversampled intensity encodes the magnitude, but not the phase, of the 3D Fourier transform of the diffracting nanocrystal. To form a strain-sensitive image of the crystal, the set of measured slices that sample the 3D coherent intensity distribution are phased using reconstruction algorithms [14] that utilize forward and inverse discrete 3D Fourier transforms ( $\mathcal{F}_{3D}$  and  $\mathcal{F}_{3D}^{-1}$ ). However, because current BCDI reconstruction approaches apply 3D discrete Fourier transforms directly to the data set, measurements that utilize these algorithms need to be performed using a fixed x-ray wavelength.

An alternative method of measuring the 3D Bragg coherent diffraction intensity distribution is to vary the length of the scattering vector  $\mathbf{q}$  while keeping the sample orientation fixed. This can be done by scanning the x-ray wavelength to change  $|\mathbf{k}|$  and  $|\mathbf{q}|$ , thus varying  $\mathbf{Q}$  as shown in Fig. 1(c) [8–10]. As compared to the monochromatic case,

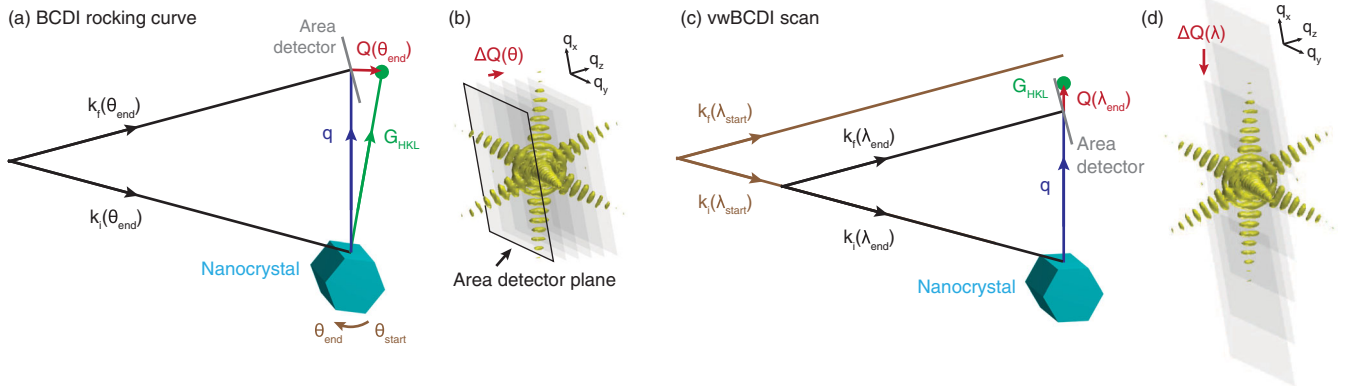


FIG. 1. This schematic depicts an isolated nanocrystal illuminated with a coherent beam and oriented such that the incident ( $\mathbf{k}_i$ ) and exit ( $\mathbf{k}_f$ ) beam wave vectors satisfy a Bragg condition for the HKL reflection (denoted by the reciprocal space vector  $\mathbf{G}_{\text{HKL}}$ ). In such an experiment, the area detector accesses a 2D slice through the 3D reciprocal space intensity pattern. To measure various components of the 3D Bragg peak intensity distribution, the scattering condition  $\mathbf{q} = \mathbf{k}_f - \mathbf{k}_i$  must be changed relative to  $\mathbf{G}_{\text{HKL}}$ , thus changing  $\mathbf{Q} = \mathbf{q} - \mathbf{G}_{\text{HKL}}$ . In a monochromatic experiment [BCDI rocking curve, panels (a) and (b)], this is done by changing the angle of the sample at a fixed  $|\mathbf{q}|$ . Alternatively, with a fixed sample position [vwBCDI scan, panels (c) and (d)], the reciprocal space volume about the Bragg peak can be sampled by changing the wavelength of the x-ray beam.

such a scan will result in a different (though equally valid) set of slices with which to assemble the 3D Bragg intensity distribution [Fig. 1(d)]. However, such a data set is not suitable for discrete  $\mathcal{F}_{3D}$ -based BCDI reconstruction algorithms because  $|\mathbf{k}|$  is not constant over the scan, and the scaling of reciprocal space in the detector changes at every measured slice. In the work featured here, this scaling changes by  $\sim 4\%$  from the beginning to the end of the scan. Without accounting for the changing wavelength in the data set, this scaling builds in an artificial asymmetry in the fringe pattern about the Bragg peak. This situation is problematic and should not be ignored in BCDI because asymmetries of this order are also indicative of lattice imperfections in the crystal [15]. Interpolation of vwBCDI data onto a regular  $\mathbf{q}$ -space grid could be performed in order to utilize current algorithms. However, typical data interpolation approaches alter the observed Poisson photon counting statistics of the underlying intensity probability distribution function [16,17] in weakly scattering regions that often convey high-spatial-resolution information.

Thus, reconstructing a 3D image from a vwBCDI measurement without interpolating intensity data requires 3D Fourier transform operations that account for the changing wavelength on a slice-by-slice basis. A related concept has been successfully implemented in reconstructing broadband forward scattering coherent diffraction patterns [18], but did not deal with the reconstruction of a reciprocal space volume. To address this challenge for the Bragg geometry, we leverage the properties of the Fourier slice projection theorem [19,20] and the relationship between spatial sampling and array size in a 2D discrete Fourier transform to define a slice-by-slice 3D Fourier transform appropriate for vwBCDI experiments. Our approach uses these concepts to perform simultaneous Fourier transformation and interpolation of each  $\lambda$ -dependent slice of the Bragg intensity distribution.

In a monochromatic BCDI scan of a Bragg peak in which  $\mathbf{Q}_j$  varies over  $j = 1, \dots, J$  two-dimensional intensity measurements, the  $j$ th 2D wave field at the detector is given by [12,13,21]:  $\psi_j = \mathcal{F}\mathcal{R}\mathcal{Q}_j\rho$ , in accordance with the Fourier slice projection theorem. In this expression,  $\mathcal{Q}_j$  is a multiplicative linear phase gradient defined as  $\mathcal{Q}_j = \exp[i\mathbf{r} \cdot \mathbf{Q}_j]$  that displaces the detector plane in reciprocal space away from Bragg peak maximum (the origin in  $\mathbf{Q}$ ).  $\mathcal{R}$  is a  $3D \rightarrow 2D$  projection along the direction of  $\mathbf{k}_f$ ,  $\mathcal{F}$  is a 2D Fourier transform, and  $\psi_j$  is the far-field exit wave in the detector. The measured intensity is then given by  $I_j = |\psi_j|^2$ .

In calculating  $\psi_j$ ,  $\mathcal{F}$  is typically implemented with a discrete 2D Fourier transform of a pixelated image array. In this case, the relationship between the pixel size in real and reciprocal space in the plane is fixed [22]. In each dimension of the projection plane, the pixel size in real space is given by  $p_{\text{samp}} = \lambda D / (N_{\text{pix}} p_{\text{det}})$ , where  $N_{\text{pix}}$  is the number of pixels along one dimension of the square array,  $p_{\text{det}}$  is the edge size of a square pixel in the area detector used in the measurement, and  $D$  is the sample-to-detector distance. In vwBCDI, we aim to maintain a constant  $p_{\text{samp}}$  for all  $\psi(\lambda_j)$ . To satisfy this condition when  $D$  and  $p_{\text{det}}$  are fixed, we can consider  $N_{\text{pix}}$  as a free parameter that varies with  $\lambda_j$  such that  $\lambda_j / N_{\text{pix}}(\lambda_j)$  is constant. So long as  $N_{\text{pix}}$  for all  $\lambda_j$  is greater than the number of pixels in the physical detector ( $N_{\text{det}}$ ), as in the case described here, then a direct comparison can be made between  $\psi(\lambda_j)$  and experimental measurements.

Based on this principle, we introduce a modified 2D Fourier transform operator  $\mathcal{F}_\lambda = S_\lambda^{-1} \mathcal{F} S_\lambda$  that maintains a constant  $p_{\text{samp}}$  by varying  $N_{\text{pix}}$ . Here,  $S_\lambda$  is an operator that pads the effective number of pixels in the array to an integer value  $N_{\text{pix}}(\lambda_j)$  that scales with  $\lambda_j$ , enforcing the appropriate

pixel sampling of each  $\psi_j$  via the discrete 2D Fourier transform. With this approach, the pixel size at the sample in the projection plane is set by experimental parameters. For a  $\lambda$  scan with a fixed step size of  $\delta\lambda$ ,  $p_{\text{samp}}$  of the real space image is given by  $(\delta\lambda)D/p_{\text{det}}$ . Additionally, the integer range of  $N_{\text{pix}}$  is set by the largest  $\lambda$  in the scan,  $N_{\text{pix}}^{\text{max}} = \lambda^{\text{max}}D/(p_{\text{samp}}p_{\text{det}})$ . Therefore, invoking  $\mathcal{S}_\lambda$  for a vwBCDI data set requires that the projection plane array be sampled with pixels of size  $p_{\text{samp}}$  and resized to  $(N_{\text{pix}}^{\text{max}} + 1 - j)$  in both dimensions for a given  $\lambda_j$ . The  $\mathcal{S}_\lambda^{-1}$  operator then resizes the array to a fixed size for all  $\lambda_j$ . In the case of  $\mathcal{F}_\lambda$ , this size is  $N_{\text{det}} \times N_{\text{det}}$ , where  $N_{\text{det}}$  is the number of physical pixels in the area detector.

Thus, the coherent wave field at the detector in a vwBCDI experiment is given by

$$\psi_j = \mathcal{F}_{\lambda_j} \mathcal{R} \mathcal{Q}_j \rho. \quad (1)$$

To better illustrate the details of this calculation, we step through these operations. To begin, we define a conjugate pair of orthogonal spatial coordinates based on the orientation of  $\mathbf{k}_f$ ,  $(r_x, r_y, r_z)$  and  $(q_x, q_y, q_z)$ . The former is the basis for the real-space vector  $\mathbf{r}$  and the latter for the reciprocal space  $\mathbf{q}$  and  $\mathbf{Q}$ . In real space, two directions  $r_x$  and  $r_y$  are normal to  $\mathbf{k}_f$  and are aligned with the edges of a square area detector [outlined in black in Fig. 1(b)]. The third direction  $r_z$  is parallel to  $\mathbf{k}_f$ .  $q_x, q_y$ , and  $q_z$  are oriented parallel to their conjugate  $r$ -space counterparts.

A visual representation of the operators in Eq. (1) is shown in Fig. 2. First, the crystal  $\rho$  is multiplied by a phase factor that depends on  $\mathbf{Q}_j$ , corresponding to a slice of the Bragg peak measured at a given  $\lambda_j$ . The complex 3D quantity  $\mathcal{Q}_j \rho$  is then projected onto the  $(r_x, r_y)$  plane, sampled with real space pixels of size  $p_{\text{samp}}$ . By

manipulating the number of pixels in the image array, the  $\mathcal{F}_{\lambda_j}$  operator adjusts the scaling of  $\psi_j$  to correspond to  $\lambda_j$ . In this way, a series of diffraction patterns  $\{\psi_1, \dots, \psi_J\}$  cutting through the Bragg intensity distribution can be generated for a scan of  $\lambda$ , as shown in Fig. 2(g).

In order to enable phase retrieval and 3D image reconstruction, a conjugate inversion procedure must be introduced that converts the reciprocal space information in  $\{\psi_1 \dots \psi_J\}$  back to real space to recover  $\rho$ . Here, we take advantage of another feature of the Fourier slice projection theorem, i.e., that a  $2\text{D} \rightarrow 3\text{D}$  backprojection operation ( $\mathcal{R}^\dagger$ ) can be used to reassemble a 3D object from a series of 2D projections. We also utilize the fact that each  $\psi_j$  is offset from the Bragg peak by  $\mathbf{Q}_j$ . The component of  $\mathbf{Q}_j$  along  $\mathbf{k}_f$  encodes the spatial frequency along  $r_z$  for the projected structural information in the  $(r_x, r_y)$  plane contained in  $\psi_j$ . Thus,  $\rho$  can be expressed by inverting the operators in Eq. (1) and summing the resulting backprojections,

$$\rho = \sum_{j=1}^J \mathcal{Q}_j^* \mathcal{R}^\dagger \mathcal{F}_{\lambda_j}^{-1} \psi_j. \quad (2)$$

In this expression,  $\mathcal{F}_{\lambda_j}^{-1} = \mathcal{S}_{\lambda_j}^{-1} \mathcal{F}^{-1} \mathcal{S}_{\lambda_j}$ , and  $\mathcal{Q}_j^* = \exp[-i\mathbf{r} \cdot \mathbf{Q}_j]$  is the complex conjugate of  $\mathcal{Q}_j$ . In this expression, we use  $\mathcal{S}_{\lambda_j}^{-1}$  to resize the real-space projection image to a size of  $N_{\text{pix}}^{\text{max}} \times N_{\text{pix}}^{\text{max}}$ .

Here, we step through the inverse operators used in Eq. (2). Starting with a given  $\psi_j$  (amplitudes and phases known),  $\mathcal{F}_{\lambda_j}^{-1}$  yields a projection of  $\mathcal{Q}_j \rho$  on the  $(r_x, r_y)$  plane with pixel size  $p_{\text{samp}}$ . Next, the backprojection operator  $\mathcal{R}^\dagger$  uniformly replicates this projection along  $r_z$ . Finally,  $\mathcal{Q}_j^*$  imparts an oscillating phase profile that encodes the appropriate spatial frequency along  $r_z$  for this slice.  $\mathcal{Q}_j^*$

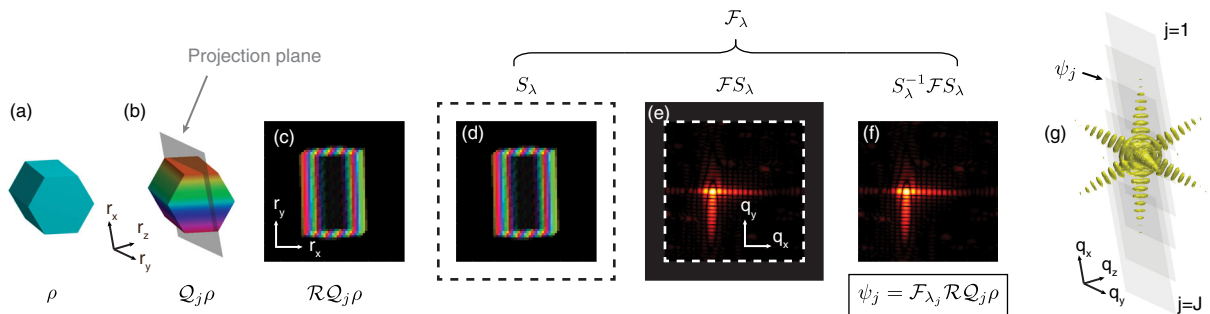


FIG. 2. Schematic of a slice-by-slice calculation of vwBCDI diffraction patterns. (a) The nanocrystal  $\rho$  is multiplied by a phase factor, resulting (b) in  $\mathcal{Q}_j \rho$ . (c) The 3D quantity  $\mathcal{Q}_j \rho$  at a given  $\lambda$  is projected onto the  $(r_x, r_y)$  plane via the projection operator  $\mathcal{R}$ . In order to properly scale the diffraction pattern for this  $\lambda$ , the operator  $\mathcal{F}_\lambda$  is invoked, defined as  $\mathcal{S}_\lambda^{-1} \mathcal{F} \mathcal{S}_\lambda$ , shown in (d)–(f). (d)  $\mathcal{S}_\lambda$  changes the number of pixels in the image to  $N_{\text{pix}}(\lambda_j)$  by padding with zeros. (e) A 2D Fourier transform  $\mathcal{F}$  of the padded projection array is applied. (f)  $\mathcal{S}_\lambda^{-1}$  resizes the resulting array back to a fixed pixel size, in this case  $N_{\text{det}} \times N_{\text{det}}$ . (g) In this manner, each slice (gray plane) through a 3D Bragg peak intensity distribution (yellow isosurface) is calculated resulting in the set  $\{\psi_1, \dots, \psi_J\}$  that mimics a vwBCDI measurement. The inverse process of reconstructing  $\rho$  from  $\{\psi_1, \dots, \psi_J\}$  involves inverting the above operators (including  $\mathcal{F}_\lambda^{-1}$ ), and is demonstrated graphically in Supplemental Fig. S1 [23].



can also encode phase gradients along  $r_x$  and  $r_y$  that account for displacement of the diffraction pattern from the central pixel of the detector at each slice. The quantity  $Q_j^* \mathcal{R}^\dagger \mathcal{F}_\lambda^{-1} \psi_j$  is calculated for all  $J$  diffraction patterns and summed. This process is visualized in Supplemental Fig. S1 for the simulated nanocrystal featured in Fig. 2(a) [23]. It is shown that as the number of summed terms approach  $J = 100$ , the morphology and phase of the summation converge to  $\rho$ .

We note that  $\mathcal{F}_\lambda$  and  $\mathcal{F}_\lambda^{-1}$  generalize the forward and inverse Fourier transform operations that describe the reciprocal space 3D volume about a Bragg peak as measured by an area detector in a variable-wavelength measurement. Effectively, when  $S_\lambda$  and  $S_\lambda^{-1}$  are unity, the operations described in Eqs. (1) and (2) are equivalent to the traditionally used forward and inverse discrete 3D Fourier transforms. Thus, by integrating them into a phase-retrieval algorithm,  $\mathcal{F}_\lambda$  and  $\mathcal{F}_\lambda^{-1}$  enable phase retrieval of vwBCDI data sets. Common phasing algorithms rely on minimizing the sum-squared error between the measured intensity distribution and the far-field exit wave of the reconstructed object,  $\epsilon^2 = \|\psi - \sqrt{I}\|^2$ . We adopt the same approach here, defining the sum-squared error as  $\epsilon^2 = \sum_j \|\psi_j - \sqrt{I_j}\|^2$ . This error metric then becomes the basis for determining a gradient  $\partial_\lambda$  for phase retrieval, after Ref. [21].

$$\partial_\lambda = \sum_{j=1}^J Q_j^* \mathcal{R}^\dagger \mathcal{F}_\lambda^{-1} \left( \psi_j - \sqrt{I_j} \frac{\psi_j}{|\psi_j|} \right). \quad (3)$$

Following Ref. [14], we obtain the modulus constraint for vwBCDI,  $P_m \rho = \rho - \frac{1}{2} \partial_\lambda$ , that enforces consistency between the amplitudes of  $\psi_{\{1, \dots, J\}}$  and the experimentally measured intensity patterns. The modulus constraint, when used in combination with an object-bounding support, is central to iterative BCDI phase-retrieval algorithms such as hybrid input or output (HIO) and error reduction (ER) [24]. (Pseudocode for ER/HIO implemented with  $\partial_\lambda$  is included in the Supplemental Material [23].) With  $\partial_\lambda$ , these reconstruction algorithms can be applied to experimental data.

To demonstrate the phase-retrieval approach introduced above, vwBCDI measurements were performed on a sub-micron-sized Au nanocrystal [25]. Measurements were performed with a mirror-focused coherent x-ray beam at the Sector 34-ID-C beam line at the Advanced Photon Source. The 111 Bragg condition was satisfied at 9 keV (far from any Au absorption edges) with a symmetric diffraction geometry (Bragg angle of  $\theta_{\text{Br}} = 17^\circ$ ). In this experiment,  $D = 0.62$  m,  $p_{\text{det}} = 55 \mu\text{m}$ , and  $N_{\text{det}} = 256$ . The scattering geometry was fixed, and the energy of the incident beam was scanned from 8.85 to 9.15 keV in 6-eV increments (corresponding to  $\delta\lambda \sim 8.9 \times 10^{-4} \text{ \AA}$  and  $\lambda^{\text{min}} = 1.378 \text{ \AA}$ ). The synchrotron undulator gap was adjusted at every energy step

in order to provide nearly constant flux at all  $\lambda_j$  [10]. Under these conditions,  $p_{\text{samp}} = 1.0 \text{ nm}$  and  $N_{\text{pix}}^{\text{max}} = 1576$  [26]. For comparison, data were also collected at 9 keV with a rocking curve ( $\theta_{\text{Br}} \pm 0.35^\circ$ ) in  $0.01^\circ$  angular increments.

HIO and ER were used with the  $\partial_\lambda$  gradient to reconstruct a 3D image of the Au crystal from the vwBCDI data, and standard  $\mathcal{F}_{3D}$ -based HIO and ER were applied to the rocking-curve data. Both data sets were successfully phased with comparable rates of convergence, and the resulting reconstructions are shown in Fig. 3. A 3D isosurface of the electron density of both reconstructions is featured, showing regions of higher lattice displacement especially near the edges and corners of  $\{111\}$  facets, as has been observed previously in gold nanoparticles prepared by thermal dewetting of films [27]. Direct comparisons of the images is difficult because the measured reciprocal space volumes and sampling of the Bragg peak from the energy and rocking scans are inherently different, leading to expected differences in the pixelation and resolution of features in the reconstructions. Nonetheless, the lattice displacements traced along equivalent lines of both reconstructions agree well [Fig. 3(e)]. We note that for larger crystals, refraction effects can become significant and should be accounted for [28].

The good agreement between the two reconstruction methods demonstrates that vwBCDI preserves the

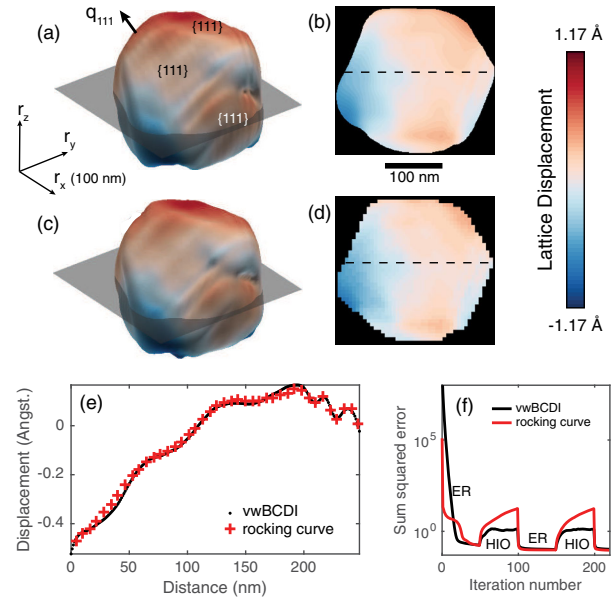


FIG. 3. (a) A density isosurface of a Au nanocrystal reconstructed using vwBCDI. Coloring corresponds to near-surface lattice displacements.  $\{111\}$  facets are labeled, and the arrow  $q_{111}$  indicates the scattering vector direction of the measured Bragg peak. (b) The lattice displacement within the nanocrystal along the gray plane in (a). (c),(d) Corresponding images of the same crystal reconstructed from rocking-curve-based BCDI data. (e) Comparison of lattice displacement lineouts along the dotted lines in (b) and (d). Error metrics from vwBCDI and standard rocking-curve phase retrieval are shown in (f).

strain-sensitive 3D imaging capability of current rocking-curve-based BCDI methods *without* requiring any sample motion. This capability will greatly simplify certain *in situ* strain measurements in environments that are difficult to accurately rotate about a precise center of rotation or that are otherwise cumbersome. The current formalism does not incorporate the energy dependence of the scattering factor. Thus, vwBCDI scans should be performed far away from absorption edges of the elements in the sample. However, enabling element-sensitive vwBCDI may be feasible with near-edge energy scanning if additional resonant scattering effects are incorporated into the phase-retrieval algorithm [29].

Development of variable x-ray wavelength transforms was supported by the U.S. Department of Energy, Office of Science, Basic Energy Sciences, Materials Sciences and Engineering Division. Creation of backprojection operators for Bragg diffraction was partially funded by the French Agence Nationale de la Recherche under Project No. ANR-11-BS10-0005. Sample preparation was supported by Engineering and Physical Sciences Research Council Grant No. EP/D052939/1. Use of the Advanced Photon Source was supported by the U.S. Department of Energy, Office of Science, Office of Basic Energy Sciences, under Contract No. DE-AC02-06CH11357. The authors gratefully acknowledge the Advanced Photon Source X-ray Science Division Optics Group for help with sample preparation.

---

\*Corresponding author.  
shrus@anl.gov

- [1] J. Li, Z. Shan, and E. Ma, *MRS Bull.* **39**, 108 (2014).
- [2] I. K. Robinson, I. A. Vartanyants, G. J. Williams, M. A. Pfeifer, and J. A. Pitney, *Phys. Rev. Lett.* **87**, 195505 (2001).
- [3] M. A. Pfeifer, G. J. Williams, I. A. Vartanyants, R. Harder, and I. K. Robinson, *Nature (London)* **442**, 63 (2006).
- [4] I. Robinson and R. Harder, *Nat. Mater.* **8**, 291 (2009).
- [5] W. Cha *et al.*, *Nat. Mater.* **12**, 729 (2013).
- [6] A. Ulvestad, A. Singer, J. N. Clark, H. M. Cho, J. W. Kim, R. Harder, J. Maser, Y. S. Meng, and O. G. Shpyrko, *Science* **348**, 1344 (2015).
- [7] J. N. Clark, L. Beitra, G. Xiong, D. M. Fritz, H. T. Lemke, D. Zhu, M. Chollet, G. J. Williams, M. M. Messerschmidt, B. Abbey *et al.*, *Proc. Natl. Acad. Sci. U.S.A.* **112**, 7444 (2015).
- [8] W. Cha, W. Liu, R. Harder, R. Xu, P. H. Fuoss, and S. O. Hruszkewycz, *J. Synchrotron Radiat.* **23**, 1241 (2016).
- [9] T. W. Cornelius, A. Davydok, V. L. R. Jacques, R. Grifone, T. Schulli, M. I. Richard, G. Beutier, M. Verdier, T. H. Metzger, U. Pietsch *et al.*, *J. Synchrotron Radiat.* **19**, 688 (2012).
- [10] T. W. Cornelius, D. Carbone, V. L. R. Jacques, T. U. Schulli, and T. H. Metzger, *J. Synchrotron Radiat.* **18**, 413 (2011).
- [11] J. Stangl, C. Mocuta, V. Chamard, and D. Carbone, *Nanobeam X-Ray Scattering: Probing Matter at the Nanoscale* (Wiley-VCH, New York, 2013).
- [12] S. O. Hruszkewycz, M. V. Holt, M. Allain, V. Chamard, S. M. Polvino, C. E. Murray, and P. H. Fuoss, *Opt. Lett.* **40**, 3241 (2015).
- [13] I. Vartanyants and I. Robinson, *J. Phys. Condens. Matter* **13**, 10593 (2001).
- [14] S. Marchesini, *Rev. Sci. Instrum.* **78**, 011301 (2007).
- [15] M. Dupraz, G. Beutier, D. Rodney, D. Mordehai, and M. Verdier, *J. Appl. Crystallogr.* **48**, 621 (2015).
- [16] P. Godard, M. Allain, V. Chamard, and J. Rodenburg, *Opt. Express* **20**, 25914 (2012).
- [17] P. Thibault and M. Guizar-Sicairos, *New J. Phys.* **14**, 063004 (2011).
- [18] B. Abbey *et al.*, *Nat. Photonics* **5**, 420 (2011).
- [19] A. C. Kak and M. Slaney, *Principles of Computerized Tomographic Imaging* (IEEE Press, New York, 1988).
- [20] F. Natterer and F. Wübbeling, *Mathematical Methods in Image Reconstruction* (SIAM, Philadelphia, 2001).
- [21] S. O. Hruszkewycz, M. Allain, M. V. Holt, C. E. Murray, J. R. Holt, P. H. Fuoss, and V. Chamard, [arXiv:1506.01262](https://arxiv.org/abs/1506.01262).
- [22] J. W. Goodman, *Introduction to Fourier Optics*, 3rd ed. (Roberts and Company, Englewood CO, 2005).
- [23] See Supplemental Material at <http://link.aps.org/supplemental/10.1103/PhysRevLett.117.225501> for a visualization of the operators associated with  $\mathcal{F}_\lambda^{-1}$ , as well as pseudocode for implementing vwBCDI with HIO and ER.
- [24] J. Fienup, *Appl. Opt.* **21**, 2758 (1982).
- [25] Samples were prepared by sputtering a layer of gold onto a single-crystal silicon substrate with a gradient of thickness ranging from 0 to 1000 nm. To form nanoparticles via thermal dewetting of the film, the coated substrate was annealed in an inert atmosphere with the following heat treatment: 1100°C for 6 hours, 1000°C for 2 hours, 900°C for 2 hours. The dewetting process resulted in gold nanocrystals of various diameters that were rigidly adhered to the silicon substrate.
- [26] We note that the formalism presented above assumes data were collected linearly in  $\lambda$ . Because of instrumental considerations, our measurement was performed with a fixed energy step that introduced variability in  $\delta\lambda$  of a few percent over the scan. Nevertheless, the measurement approximated a linear  $\lambda$  scan sufficiently so as to demonstrate the principle here.
- [27] M. Watari, R. A. McKendry, M. Vogtli, G. Aeppli, Y.-A. Soh, X. Shi, G. Xiong, X. Huang, R. Harder, and I. K. Robinson, *Nat. Mater.* **10**, 862 (2011).
- [28] R. Harder, M. A. Pfeifer, G. J. Williams, I. A. Vartanyants, and I. K. Robinson, *Phys. Rev. B* **76**, 115425 (2007).
- [29] S. T. Haag, M.-I. Richard, S. Labat, M. Gailhanou, U. Welzel, E. J. Mittemeijer, and O. Thomas, *Phys. Rev. B* **87**, 035408 (2013).